Research Square

Preprints are preliminary reports that have not undergone peer review.
They should not be considered conclusive, used to inform clinical practice,
or referenced by the media as validated information.

Band-dependent charging governs electrochemical energetics in two-dimensional materials

Xin Tan

xintan@wzu.edu.cn

Wenzhou University https://orcid.org/0000-0001-9515-2346

Tingfuyu Liu

Wenzhou University

Ping Tong

Wenzhou University

Dan Lu

Wenzhou University

Qianxiong Wen

Wenzhou University

Xingqiao Wu

Wenzhou University

Yihong Ding

Shanghai University

Shulei Chou

Wenzhou University https://orcid.org/0000-0003-1155-6082

Liangzhi Kou

School of Mechanical, Medical and Process Engineering, Queensland University of Technology
https://orcid.org/0000-0002-3978-117X

Article

Keywords:

Posted Date: November 24th, 2026

DOI: https://doi.org/10.21203/rs.3.rs-11836229/v1

License: This work is licensed under a Creative Commons Attribution 4.0 International License.
Read Full License

Additional Declarations: There is **NO** Competing Interest.

Band-dependent charging governs electrochemical energetics in two-dimensional materials

Xin Tan[1,3,4]*, Tingfuyu Liu[1], Ping Tong[1], Dan Lu[1], Qianxiong Wen[1], Xingqiao Wu[1,3,4]*, Yihong Ding[1], Shulei Chou[1,3,4]*, Liangzhi Kou[2]*

[1] Institute for Carbon Neutralization Technology, College of Chemistry and Materials Engineering, Wenzhou University, Wenzhou, Zhejiang 325035, China

[2] School of Mechanical, Medical and Process Engineering Faculty, Queensland University of Technology, Brisbane, QLD, Australia

[3] Zhejiang Provincial Key Laboratory of Advanced Battery Materials and Technology, Wenzhou University Technology Innovation Institute for Carbon Neutralization, Wenzhou, Zhejiang 325035, China

[4] Zhejiang-Australia International Joint Laboratory for Sodium-Ion Batteries Wenzhou University Technology Innovation Institute for Carbon Neutralization Wenzhou, Zhejiang 325035, China

* Corresponding authors. E-mail: xintan@wzu.edu.cn; xingqiaowu@wzu.edu.cn; chou@wzu.edu.cn; liangzhi.kou@qut.edu.au

Abstract

Accurately predicting the electrochemical energetics of two-dimensional (2D) materials as electrode potential varies is critical for understanding interfacial processes underlying electrocatalysis and rechargeable batteries. However, the conventional single-quadratic model (CSQM), widely used for metallic/semimetallic systems, cannot capture distinct charging behaviors arising from separated valence and conduction bands in semiconductors. Here, we reveal band-dependent charging as a general feature of 2D materials and establish its connection to their intrinsic electronic characteristics. We therefore develop a dual-quadratic model (DQM) that separately captures valence- and conduction-band charging behaviors, enabling continuous prediction of potential-dependent energetics across metallic, semimetallic, and semiconducting 2D materials. Using only 6 discrete grand canonical density functional theory (GC-DFT) calculations, the DQM predicts potential-dependent adsorption energy profiles matching densely sampled GC-DFT benchmarks (RMSE ~ 0.055 eV), whereas the CSQM exhibits errors of up to 80%. These findings establish band-dependent charging as a governing principle of electrochemical energetics in 2D materials.

Introduction

Two-dimensional (2D) materials have emerged as versatile platforms for electrochemical energy conversion and storage owing to their atomic-scale thickness, structural tunability, and diverse electronic properties spanning metallic, semimetallic, and semiconducting states[1–3]. Representative systems include graphene,[4–6] MXenes,[7–9] transition-metal dichalcogenides (TMDs),[10–12] and layered oxides[13–15]. Under electrochemical conditions, varying the applied electrode potential (U) shifts the Fermi level (E_F), driving electron accumulation or depletion and thereby inducing potential-dependent charging that modulates the electronic structures and electrochemical energetics of 2D materials[16,17]. Such charging directly links U to material energetics, influencing interfacial processes ranging from adsorbate binding and reaction energetics in electrocatalysis to ion insertion and storage in rechargeable batteries[16,17]. Therefore, quantitatively descripting potential-dependent charging and its effects on electrochemical energetics is essential for understanding how U controls the energetics of 2D materials.

Standard density functional theory (DFT) calculations are typically performed for systems with a fixed number of electrons and cannot explicitly capture potential-dependent charging under electrochemical conditions[18–20]. Grand canonical DFT (GC-DFT) calculations overcome this limitation by allowing electron exchange with an electron reservoir at a fixed U, enabling quantitative characterization of charging at discrete potentials[16,17,21]. In recent years, GC-DFT calculations have emerged as a powerful computational approach for investigating potential-dependent interfacial processes, with applications in electrocatalysis[22–33] and rechargeable batteries[34–36].

In principle, GC-DFT calculations with dense potential sampling can enable quantitative characterization of charging and electrochemical energetics across a continuous potential range. However, the high computational cost of GC-DFT makes dense sampling impractical across diverse materials, limiting its broader application. This challenge calls for analytical models that can enable continuous prediction of potential-dependent energetics from a limited number of discrete GC-DFT calculations

while capturing the underlying physics of material charging. The conventional single-quadratic model (CSQM) is a widely adopted analytical framework for describing potential-dependent energetics based on an approximately quadratic energy–potential relationship[37,38]. Its simplicity and computational efficiency have made it particularly suitable for metallic/semimetallic materials, where continuous electronic states near the charge-neutral Fermi level (E_F^0) support smoothly varying charging over a broad potential range[22–33].

However, whether this single quadratic relationship remains valid for semiconducting 2D materials with finite band gaps remains unclear. Our densely sampled GC-DFT calculations reveal that band-dependent charging is a general feature of 2D materials, with its manifestation determined by their intrinsic electronic characteristics (Fig. 1b). In metallic/semimetallic systems, band-dependent charging manifests as effectively single-quadratic charging behavior, whereas semiconducting systems exhibit distinct valence- and conduction-band charging behaviors. Although the CSQM adequately describes single-quadratic charging behavior in metallic/semimetallic systems, it cannot capture the distinct valence- and conduction-band charging behaviors of semiconducting systems, highlighting a fundamental limitation of this conventional model (Fig. 1c). Addressing this limitation requires a general analytical model that captures band-dependent charging and enables continuous prediction of potential-dependent energetics across diverse 2D materials.

Here, we develop a dual-quadratic model (DQM) that separately describes valence- and conduction-band charging behaviors, enabling continuous prediction of potential-dependent energetics across metallic, semimetallic, and semiconducting 2D materials. Using only 6 discrete GC-DFT calculations for parameterization, the DQM accurately predicts potential-dependent adsorption energy profiles in close agreement with densely sampled GC-DFT benchmarks, substantially reducing the computational cost while capturing band-dependent charging in semiconducting systems that the CSQM cannot describe. These findings establish band-dependent charging as a general principle

governing potential-dependent energetics and reveal how intrinsic electronic characteristics shape charging behavior across 2D materials.

Results and discussion

Band-dependent charging as a general principle in 2D materials

Under electrochemical conditions, variations in U drive electron exchange between 2D materials and the electrode, shifting the material's E_F and altering its charge state[16,17]. As illustrated in Fig. 1a, the charge state depends on U relative to E_F^0. At $U = E_F^0$, the material remains charge neutral. Lowering U below E_F^0 induces electron accumulation and negative charging, whereas raising U above E_F^0 promotes electron depletion and positive charging. Thus, variations in U modulate the charge state and electronic structure, giving rise to potential-dependent charging across diverse 2D materials.

To establish reliable benchmarks for potential-dependent charging, we performed densely sampled GC-DFT calculations of the grand canonical energy ($E_{GC}(U)$) at 0.5 V intervals over a broad potential range for two representative 2D systems with contrasting intrinsic electronic characteristics: semimetallic Fe–N–C and semiconducting MoS_2 (Fig. 1b). The potential range spans several volts around 0 V versus the standard hydrogen electrode (SHE), covering potential regimes relevant to electrochemical processes in electrocatalysis[39–41] and rechargeable batteries[42–44] (Fig. 1a). Although computationally demanding and impractical for large-scale screening, these densely sampled GC-DFT calculations resolve material-specific charging behavior in detail and provide reference profiles for validating analytical models.

As shown in Fig. 1b, the $E_{GC} - U$ relationships obtained from densely sampled GC-DFT benchmarks reveal contrasting charging behaviors in semimetallic Fe–N–C and semiconducting MoS_2. For Fe–N–C, E_{GC} varies smoothly across the full potential range, consistent with single-quadratic charging behavior[28,30]. In contrast, MoS_2 exhibits distinct charging behaviors in its valence- and conduction-band regimes. These results demonstrate that potential-dependent charging in 2D materials is inherently band-dependent, with its manifestation depending on their intrinsic electronic characteristics.

However, the band-dependent charging has remained largely unexplored in existing analytical descriptions of potential-dependent electrochemical energetics, which have predominantly focused on metallic/semimetallic systems, particularly graphene-based materials[22,24,28–30].

The CSQM has been widely adopted as a simple and computationally efficient analytical framework for describing potential-dependent charging in 2D materials, assuming a single quadratic relationship between E_{GC} and U. Specifically, a single quadratic function is fitted to $E_{\mathrm{GC}}(U)$ values obtained from a limited number of discrete GC-DFT calculations, typically 5–6 potential points, enabling continuous prediction of the $E_{\mathrm{GC}} - U$ relationship[37,38]:

$$E_{\mathrm{GC}}(U) = -0.5C(U - U_{\mathrm{PZC}})^2 + E_0 \quad (1)$$

where C is the capacitance, U_{PZC} is the potential of zero charge, and E_0 is the grand canonical energy at U_{PZC}. This approximately quadratic dependence arises from the capacitor-like charging picture underlying the CSQM, in which charge accumulation or depletion in the slab is compensated by a uniform background charge. As shown in Fig. 1c, for semimetallic Fe–N–C, the CSQM reproduces the single-quadratic $E_{\mathrm{GC}} - U$ relationship obtained from the densely sampled GC-DFT benchmark, consistent with previous applications to metallic/semimetallic systems[22,24,28-30]. In contrast, for semiconducting MoS_2, the CSQM deviates substantially from the densely sampled GC-DFT benchmark, particularly near $U = E_{\mathrm{F}}^0$. This discrepancy reflects the inability of a single quadratic function to capture the distinct valence- and conduction-band charging behaviors in semiconductors. These limitations motivate a generalized analytical model that can describe band-dependent charging across 2D materials with diverse intrinsic electronic characteristics.

A dual-quadratic model for band-dependent charging

The distinct charging behaviors of MoS_2 in the two charging regimes provide a basis for separately analyzing their $E_{\mathrm{GC}} - U$ relationships, with valence-band charging occurring at $U > E_{\mathrm{F}}^0$ and conduction-band charging at $U < E_{\mathrm{F}}^0$ (Fig. 1b). Within each

regime, E_{GC} varies smoothly with U, suggesting that each branch can be described by an individual analytical function. Notably, both branches exhibit an approximately quadratic dependence on U, consistent with the quadratic form assumed in the CSQM. However, a single quadratic function across the full potential range cannot adequately capture the distinct charging behaviors in MoS_2. We therefore develop the DQM by independently parameterizing the valence- and conduction-band branches as follows:

$$E_{\mathrm{GC}}^{\mathrm{VB}}(U) = -0.5C_{\mathrm{VB}}\left(U - U_{\mathrm{PZC,VB}}\right)^2 + E_{0,\mathrm{VB}} \qquad (U > E_{\mathrm{F}}^0) \tag{2}$$

$$E_{\mathrm{GC}}^{\mathrm{CB}}(U) = -0.5C_{\mathrm{CB}}\left(U - U_{\mathrm{PZC,CB}}\right)^2 + E_{0,\mathrm{CB}} \qquad (U < E_{\mathrm{F}}^0) \tag{3}$$

where $E_{\mathrm{GC}}^{\mathrm{VB}}(U)$ and $E_{\mathrm{GC}}^{\mathrm{CB}}(U)$ denote the grand canonical energies at U for the valence- and conduction-band branches, respectively. C_{VB} and C_{CB} are the associated capacitances. $U_{\mathrm{PZC,VB}}$ and $U_{\mathrm{PZC,CB}}$ are the corresponding potentials of zero charge. $E_{0,\mathrm{VB}}$ and $E_{0,\mathrm{CB}}$ are the grand canonical energies at $U_{\mathrm{PZC,VB}}$ and $U_{\mathrm{PZC,CB}}$, respectively.

We first applied the DQM to two representative 2D materials with contrasting intrinsic electronic characteristics: semimetallic Fe–N–C and semiconducting MoS_2. For both materials, the DQM reproduces the $E_{\mathrm{GC}} - U$ relationships obtained from densely sampled GC-DFT benchmarks across the full potential range (Fig. 1d). We then evaluated its broader applicability using four additional 2D materials spanning metallic, semimetallic, and semiconducting systems: N-doped graphene with single-vacancy (1V_N) and pore-containing (P_N) configurations, MnO_2, and Ti_2C (Fig. 2a–e). Across all six materials, the DQM consistently agrees with the densely sampled GC-DFT benchmarks (Supplementary Fig. 1) and outperforms the CSQM (Supplementary Fig. 2). These results demonstrate that the DQM reliably captures band-dependent charging across diverse 2D materials.

Comparison of the DQM-predicted $E_{\mathrm{GC}} - U$ relationships across the six materials reveals two types of branch configurations (Fig. 2f). In semiconducting systems (MnO_2 and MoS_2), the valence- and conduction-band branches exhibit nearly identical curvatures but are clearly separated along the potential axis, give rise to distinct valence- and conduction-band charging behaviors. By contrast, in metallic/semimetallic systems (1V_N, Fe–N–C, P_N, and Ti_2C), the two branches

nearly overlap, yielding an effectively single-quadratic charging behavior. These contrasting branch configurations correlate with the intrinsic electronic characteristics of the materials, pointing to the electronic origin of band-dependent charging.

Electronic origin of band-dependent charging in 2D materials

A key difference between semiconducting and metallic/semimetallic materials lies in the electronic states near E_{F}^{0}. Semiconductors possess a finite band gap (E_{g}) separating the valence and conduction bands, whereas metallic/semimetallic materials exhibit continuous electronic states across E_{F}^{0}. To quantify the separation between the valence- and conduction-band branches in the DQM, we define their potential offset as $\Delta U_{\mathrm{PZC}} = U_{\mathrm{PZC,VB}} - U_{\mathrm{PZC,CB}}$. Comparing ΔU_{PZC} with E_{g}, extracted from the calculated total density of states (TDOS), reveals an approximately linear relationship with a slope of ~1.10 (Fig. 3a).

This scaling establishes a quantitative connection between the intrinsic electronic characteristics of the materials and the separation of the DQM branches along the potential axis. In semiconducting materials, a finite E_{g} corresponds to a non-negligible ΔU_{PZC}, separating the valence- and conduction-band branches along the potential axis (Fig. 3b). Shifting the conduction-band branch by ΔU_{PZC} brings the two branches into near-complete overlap, recovering a single quadratic dependence on potential (Fig. 3c and Supplementary Fig. 3). This overlap indicates that the two branches share the same quadratic form but are offset along the potential axis by ΔU_{PZC}, with the offset reflecting E_{g} rather than fundamentally distinct charging behaviors. Conversely, in metallic/semimetallic materials, the vanishing E_{g} is accompanied by a negligible ΔU_{PZC}, so the two DQM branches nearly overlap and collectively exhibit effectively single-quadratic charging behavior described by the CSQM (Fig. 3b).

Band-dependent charging underlies potential-dependent adsorption energetics

Because adsorption energetics at electrochemical interfaces are coupled to substrate charging, band-dependent charging is expected to have important implications for their potential dependence. To investigate this effect, we systematically evaluated the potential-dependent adsorption energies ($E_{\mathrm{ads}}(U)$) of nine adsorbates (H_2O, CO, O, H, N, S, Li, Na, and Mg) across six 2D materials spanning metallic, semimetallic, and semiconducting characteristics. These adsorbates were selected to represent diverse interfacial processes relevant to electrocatalysis[39–41] and rechargeable batteries[42–44].

To quantify the coupling between substrate charging and adsorption energetics, we employ the energy decomposition scheme established in our previous work[34], which separates the $E_{\mathrm{ads}}(U)$ into a charge-induced electronic contribution ($E_{\mathrm{ele}}(U)$) and a charge-induced structural relaxation contribution ($E_{\mathrm{rel}}(U)$) (Fig. 4a):

$$E_{\mathrm{ads}}(U) = E_{\mathrm{ele}}(U) + E_{\mathrm{rel}}(U) \quad (4)$$

where $E_{\mathrm{ele}}(U)$ represents the electronic contribution to the adsorption energy induced by charging, evaluated with the adsorbed system fixed at its charge-neutral configuration. $E_{\mathrm{rel}}(U)$ is the additional energy change arising from structural relaxation between the charge-neutral and charged configurations. Calculation details for $E_{\mathrm{ele}}(U)$, $E_{\mathrm{rel}}(U)$ and $E_{\mathrm{ads}}(U)$ are provided in Supplementary Note 1.

We first compared the DQM and CSQM in predicting $E_{\mathrm{ele}}(U)$. Densely sampled GC-DFT calculations provided benchmark $E_{\mathrm{ele}}(U)$ profiles across the full potential range. The DQM and CSQM were independently parameterized using discrete GC-DFT calculations for both bare substrates and adsorbed systems, and subsequently used to predict their $E_{\mathrm{GC}} - U$ relationships. $E_{\mathrm{ele}}(U)$ predictions were obtained by subtracting the bare-substrate $E_{\mathrm{GC}} - U$ predictions from those of the adsorbed systems. These results were then compared with the benchmark $E_{\mathrm{ele}}(U)$ profiles to assess the accuracy of the two analytical models. Details of the DQM and CSQM prediction of $E_{\mathrm{ele}}(U)$ profiles are provided in Supplementary Note 2.

Across all investigated adsorbed systems, the DQM-predicted $E_{\mathrm{ele}}(U)$ profiles closely matched the benchmark profiles across the full potential range, reproducing both the magnitude and curvature of the potential dependence (Fig. 4d–h and

Supplementary Figs. 4–6). This agreement held across metallic, semimetallic, and semiconducting 2D materials, demonstrating the broad applicability of the DQM in capturing the electronic contribution to potential-dependent adsorption energetics through an explicit treatment of band-dependent charging. By contrast, the CSQM deviates substantially from the benchmark $E_{\mathrm{ele}}(U)$ profiles for semiconducting systems, particularly near the band-gap region, where its single-quadratic form fails to capture the distinct valence- and conduction-band charging behaviors.

H_2O adsorption on MnO_2 provides a representative comparison of the DQM and CSQM (Fig. 4b–d). For both bare MnO_2 and H_2O-adsorbed MnO_2, the DQM reproduced the $E_{\mathrm{GC}} - U$ relationships from densely sampled GC-DFT benchmarks (Fig. 4b), resulting in near-quantitative agreement between the predicted $E_{\mathrm{ele}}(U)$ profile and the benchmark profile (RMSE = 0.003 eV, Fig. 4d). By contrast, the CSQM-predicted $E_{\mathrm{GC}} - U$ relationships exhibited substantial deviations for both systems (Fig. 4b), leading to systematic overestimation of $E_{\mathrm{ele}}(U)$ and a relatively higher RMSE of 0.055 eV. At U_{SHE} = 4.0 V, for example, the CSQM predicted $E_{\mathrm{ele}}(U) = -0.37$ eV, compared with the benchmark GC-DFT value of -0.21 eV, corresponding to a relative error of 76% (Fig. 4d).

We next examined the relative contribution of charge-induced structural relaxation using the ratio $E_{\mathrm{rel}}(U)/|E_{\mathrm{ele}}(U)|$, which measures the magnitude of the structural relaxation contribution relative to that of the electronic contribution. Across the six 2D materials and nine adsorbates, this ratio varied substantially in both magnitude and potential dependence (Fig. 5 and Supplementary Figs. 7–9). Li and CO adsorption on MnO_2 illustrate two contrasting cases. For Li adsorption (Fig. 5a), the ratio remained close to zero across the full potential range, indicating that structural relaxation contributes negligibly to the adsorption energetics. By contrast, for CO adsorption, the ratio became increasingly negative as U decreased, reaching -0.92 at $U_{\mathrm{SHE}} = -3.0$ V (Fig. 5b). This result demonstrates that under strongly negative charging conditions, the

structural relaxation contribution can become comparable in magnitude to the electronic contribution.

To explain the larger structural relaxation contribution for CO than for Li adsorption on MnO_2, we examined the potential-dependent deviation of the adsorbate charge from its charge-neutral state, $Q(U) - Q_{\mathrm{CN}}$. Under strongly negative charging conditions (U_{SHE} < 1.0 V), CO exhibited substantially greater charge redistribution than Li (Fig. 5a,b), consistent with its larger structural relaxation contribution. This enhanced charge redistribution strengthens electrostatic interactions at the adsorbate–MnO_2 interface, leading to more pronounced structural rearrangements.

Finally, we combined $E_{\mathrm{ele}}(U)$ and $E_{\mathrm{rel}}(U)$ to reconstruct $E_{\mathrm{ads}}(U)$ and compared the DQM and CSQM predictions with the benchmark profiles. For systems with both negligible and substantial structural relaxation contributions (Fig. 5a,b), the DQM reproduced the benchmark $E_{\mathrm{ads}}(U)$ profiles across the full potential range, demonstrating its accuracy regardless of the extent of charge-induced structural relaxation. Across all investigated adsorbed systems, the DQM consistently outperformed the CSQM, capturing both the energy values and potential-dependent trends of the benchmark $E_{\mathrm{ads}}(U)$ profiles (Fig. 5a–d and Supplementary Figs. 10–12). These results establish the DQM as a general analytical framework for predicting potential-dependent adsorption energetics, incorporating both electronic and structural relaxation contributions induced by charging.

Sparse GC-DFT sampling enables efficient prediction of potential-dependent adsorption energetics

The efficiency of continuously predicting potential-dependent adsorption energetics depends critically on the number of discrete GC-DFT calculations required for model parameterization. Insufficient GC-DFT sampling may compromise prediction accuracy, whereas excessive sampling increases computational cost and diminishes the efficiency advantage of analytical models. An effective model must balance predictive accuracy against the number of GC-DFT sampling points. To evaluate this trade-off, we

systematically increased the number of discrete GC-DFT calculations used to parameterize the DQM and CSQM and compared their predictions with densely sampled GC-DFT benchmarks (Fig. 6a,b and Supplementary Figs. 13,14).

CO adsorption on MnO_2 was selected as a representative case to evaluate the sampling efficiency of the DQM (Fig. 6b and Supplementary Fig. 14). The DQM-predicted $E_{\mathrm{ads}}(U)$ profile converged with only 6 discrete GC-DFT calculations, with 3 points assigned to each quadratic branch, yielding a low RMSE of 0.055 eV. Further increasing the sampling density to 16 points brought negligible improvement, indicating that 6-point parameterization is sufficient to accurately predict potential-dependent adsorption energetics. As shown in Fig. 6c, the 6-point and 16-point DQM predictions nearly overlap, both reproducing the benchmark $E_{\mathrm{ads}}(U)$ profile across the full potential range. This sampling efficiency follows directly from the DQM formulation, which requires 3 independent parameters to define each quadratic branch. In contrast, the CSQM yielded an RMSE of 0.104 eV even with 16 discrete GC-DFT calculations (Fig. 6b and Supplementary Fig. 14). This persistent discrepancy indicates that increasing sampling density cannot overcome the intrinsic limitation of the CSQM, which relies on a single quadratic function to represent band-dependent charging.

We further assessed the generality of the 6-point DQM across diverse adsorbates on metallic, semimetallic, and semiconducting 2D materials (Fig. 6d,e and Supplementary Figs.15–17). The model consistently reproduced the benchmark $E_{\mathrm{ads}}(U)$ profiles across all investigated systems, despite differences in their potential-dependent charging behaviors. These results establish the broad applicability of the 6-point DQM for continuously predicting potential-dependent adsorption energetics across diverse 2D materials with sparse GC-DFT sampling.

Conclusions

In summary, this work reveals band-dependent charging as a general feature of 2D materials, with its manifestation determined by their intrinsic electronic characteristics. In metallic/semimetallic systems, band-dependent charging manifests as an effectively

single-quadratic dependence on potential, whereas finite band gaps in semiconducting systems give rise to distinct valence- and conduction-band charging behaviors that the CSQM cannot capture. Building on this insight, we developed the DQM to separately describe valence- and conduction-band charging behaviors, enabling continuous prediction of potential-dependent energetics from discrete GC-DFT calculations across metallic, semimetallic, and semiconducting 2D materials. Using only 6 discrete GC-DFT calculations, the DQM reproduced the benchmark $E_{\mathrm{ads}}(U)$ profiles with an RMSE of approximately 0.055 eV, whereas the CSQM exhibited relative errors of up to 80%. These results establish the DQM as an accurate and computationally efficient framework for predicting potential-dependent adsorption energetics. More broadly, this work identifies band-dependent charging as a governing principle of electrochemical energetics, linking the intrinsic electronic characteristics of 2D materials to their potential-dependent charging and adsorption energetics. This insight provides a general basis for understanding and predicting electrochemical energetics across diverse 2D materials.

Methods

DFT calculations

All spin-polarized DFT calculations were carried out using the Vienna ab initio simulation package (VASP)[45,46]. The core–valence interactions were described using the projector augmented wave (PAW) method[47,48] and the electronic wavefunctions were expanded in a plane-wave basis set. The generalized gradient approximation with the Perdew–Burke–Ernzerhof (GGA-PBE) exchange–correlation functional[49] was employed, together with Grimme's DFT-D3 dispersion correction[50,51] to account for long-range van der Waals interactions. The on-site Hubbard U_{Hub} correction was applied to describe the localized 3d electrons, using values of 3.29 eV for Fe in Fe–N–C and 3.90 eV for Mn in MnO_2, as reported in previous studies[52,53]. A plane-wave energy cutoff of 450 eV was used after convergence testing. Structural relaxations were performed until the maximum residual force on any atom fell below 0.02 eV $Å^{-1}$, with

the total energy convergence criterion set to 10^{-5} eV. Brillouin-zone integrations were performed using a Γ-centered 5 × 5 × 1 *k*-point mesh for geometry optimizations and a denser 10 × 10 × 1 *k*-point mesh for DOS calculations[54]. Bader charge analysis was performed to quantify the excess electron population on adsorbates in both charge-neutral and potential-dependent charged states[55,56].

Structural models

Six representative 2D materials were constructed using periodic slab models, including single-layer 5 × 5 graphene, 4 × 4 MnO_2, 4 × 4 MoS_2, and 4 × 4 Ti_2C. Defective and doped graphene-based structures, namely 1V_N, P_N, and Fe–N–C, were generated by removing C atoms and introducing N and Fe atoms into the graphene lattice. Adsorption configurations were constructed by placing H_2O and CO molecules, as well as O, H, N, S, Li, Na, and Mg atoms, on the surfaces of these 2D materials. A vacuum layer of approximately 18 Å was introduced along the *z* direction to minimize spurious interactions between periodic images of the slabs.

GC-DFT calculations

Potential-dependent charging under electrochemical conditions was treated explicitly using GC-DFT calculations implemented in the CP-VASP code[28,30,34-36]. Solvation effects were described using the implicit solvation model in VASPsol[57,58], which solves the linearized Poisson–Boltzmann equation. The relative permittivity of the vacuum region was set to 1.0. In CP-VASP, the electron chemical potential (μ_e) was determined by *U* relative to the SHE:

$$\mu_e = \Phi_{SHE} - |e|U \quad (5)$$

where Φ_{SHE} is the work function of the SHE in VASPsol (-4.6 eV)[34,35,58]. The electron number is adjusted self-consistently to maintain the fixed μ_e. The $E_{GC}(U)$ at a given *U* was calculated as:

$$E_{GC}(U) = E_{DFT} - \mu_e[q(U) - q_{CN}] \quad (6)$$

where E_{DFT} is the standard VASP total energy, and q_{CN} and $q(U)$ denote the electron numbers in the charge-neutral state and at U, respectively.

Data availability

All data generated in this study are provided in the main text, figures, and Supplementary Information, or from the corresponding authors upon request.

Online content

Any methods, additional references, Nature Portfolio reporting summaries, source data, extended data, supplementary information, acknowledgements, peer review information; details of author contributions and competing interests; and statements of data and code availability are available at https://doi.org/.

References

1. Liu, F. & Fan, Z. Defect engineering of two-dimensional materials for advanced energy conversion and storage. *Chem. Soc. Rev.* **52**, 1723–1772 (2023).
2. Tao, H. et al. Two-dimensional materials for energy conversion and storage. *Prog. Mater Sci.* **111**, 100637 (2020).
3. Chia, X. & Pumera, M. Characteristics and performance of two-dimensional materials for electrocatalysis. *Nat. Catal.* **1**, 909–921 (2018).
4. Novoselov, K. S. et al. Electric field effect in atomically thin carbon films. *Science* **306**, 666-669 (2004).
5. Geim, A. K. & Novoselov, K. S. The rise of graphene. *Nat. Mater.* **6**, 183–191 (2007).
6. El-Kady, M., Shao, Y. & Kaner, R. B. Graphene for batteries, supercapacitors and beyond. *Nat. Rev. Mater.* **1**, 16033 (2016).
7. Li, X. et al. MXene chemistry, electrochemistry and energy storage applications. *Nat. Rev. Chem.* **6**, 389–404 (2022).

8. Anasori, B., Lukatskaya, M. R. & Gogotsi, Y. 2D metal carbides and nitrides (MXenes) for energy storage. *Nat. Rev. Mater.* **2**, 16098 (2017).
9. Pang, J. et al. Applications of 2D MXenes in energy conversion and storage systems. *Chem. Soc. Rev.* 48, **72–133** (2019).
10. Chhowalla, M. et al. The chemistry of two-dimensional layered transition metal dichalcogenide nanosheets. *Nat. Chem.* **5**, 263–275 (2013).
11. Roy, S. et al. Engineered two-dimensional transition metal dichalcogenides for energy conversion and storage. *Chem. Rev.* **124**, 9376–9456 (2024).
12. Wu, X., Zhang, H., Zhang, J. & Lou, X. W. Recent advances on transition metal dichalcogenides for electrochemical energy conversion. *Adv. Mater.* **33**, 2008376 (2021).
13. Yuan, D. et al. Atomically thin materials for next-generation rechargeable batteries. *Chem. Rev.* **122**, 957–999 (2022).
14. Browne, M. P., Sofer, Z. & Pumera, M. Layered and two dimensional metal oxides for electrochemical energy conversion. *Energy Environ. Sci.* **12**, 41–58 (2019).
15. Zhao, Q. et al. Preintercalation strategy in manganese oxides for electrochemical energy storage: review and prospects. *Adv. Mater.* **32**, 2002450 (2020).
16. Levell, Z. et al. Emerging atomistic modeling methods for heterogeneous electrocatalysis. *Chem. Rev.* **124**, 8620−8656 (2024).
17. Zhao, X., Levell, Z. H., Yu, S. & Liu, Y. Atomistic understanding of two-dimensional electrocatalysts from first principles. *Chem. Rev.* **122**, 10675−10709 (2022).
18. Nørskov, J., Bligaard, T., Rossmeisl, J. & Christensen, C. H. Towards the computational design of solid catalysts. *Nat. Chem.* **1**, 37–46 (2009).
19. Ceder, G. et al. Identification of cathode materials for lithium batteries guided by first-principles calculations. *Nature* **392**, 694–696 (1998).
20. Islam, M. S. & Fisher, C. A. J. Lithium and sodium battery cathode materials: computational insights into voltage, diffusion and nanostructural properties. *Chem. Soc. Rev.* **43**, 185–204 (2014).

21. Sundararaman, R., Goddard, W. A. III & Arias, T. A. Grand canonical electronic density-functional theory: algorithms and applications to electrochemistry. *J. Chem. Phys.* **146**, 114104 (2017).
22. Zhang, J., Wang, Y. & Li, Y. Potential-modulated orbital interactions determine domino CO/methanol selectivity for CO_2 electroreduction on cobalt phthalocyanine. *Sci. Adv.* **11**, eadz9944 (2025)
23. Ringe S. The importance of a charge transfer descriptor for screening potential CO_2 reduction electrocatalysts. *Nat. Commun.* **14**, 2598 (2023).
24. Hossain, M. D., Huang, Y., Yu, T. H., Goddard, W. A. III & Luo, Z. Reaction mechanism and kinetics for CO_2 reduction on nickel single atom catalysts from quantum mechanics. *Nat. Commun.* **11**, 2256 (2020).
25. Tian, Y. et al. Theoretical insights on potential-dependent oxidation behaviors and antioxidant strategies of MXenes. *Nat. Commun.* **15**, 10099 (2024).
26. Cheng, D. et al. Structure sensitivity and catalyst restructuring for CO_2 electro-reduction on copper. *Nat. Commun.* **16**, 4064 (2025).
27. Wu, F. et al. Identification of K^+-determined reaction pathway for facilitated kinetics of CO_2 electroreduction. *Nat. Commun.* **15**, 6972 (2024).
28. Levell, Z., Yu, S., Wang, R. & Liu, Y. What is the "other" site in M-N-C? *J. Am. Chem. Soc.* **147**, 603–609 (2025).
29. Liu, T., Xu, T., Li, T. & Jing, Y. Selective CO_2 reduction over γ-graphyne supported single-atom catalysts: crucial role of strain regulation. *J. Am. Chem. Soc.* **146**, 24133−24140 (2024).
30. Cui, Y. et al. Structure-stability relation of single-atom catalysts under operating conditions of CO_2 reduction. *J. Am. Chem. Soc.* **146**, 29169–29176 (2024).
31. Cui, Y. et al. Beyond local coordination: how global structure engineers the selectivity of single atom catalysts for CO_2 reduction. *Angew. Chem. Int. Ed.* **65**, e19826 (2026).

462 32. Osella, S. & Goddard, W. A. III. CO_2 reduction to methane and ethylene on a
463 single-atom catalyst: a grand canonical quantum mechanics study. *J. Am. Chem.*
464 *Soc.* **145**, 21319−21329 (2023).
465 33. Yu, S., Levell, Z., Jiang, Z., Zhao, X. & Liu, Y. What is the rate-limiting step of
466 oxygen reduction reaction on Fe−N−C catalysts? *J. Am. Chem. Soc.* **145**,
467 25352−25356 (2023).
468 34. Tan, X. et al. Origin of reversible interlayer-disorder-induced phase transitions in
469 layered sodium manganese oxide cathodes. *J. Am. Chem. Soc.* **148**, 26434–26445
470 (2026).
471 35. Tan, X. et al. Critical role of potential-driven charge effects in hard carbon anodes
472 for sodium storage. *Angew. Chem. Int. Ed.* **64**, e202512830 (2025).
473 36. Liu, T. et al. Revisiting sodium storage mechanisms in closed-pore hard carbons:
474 nucleation vs. clustering under potential-driven charge effects. *J. Energy Chem.*
475 **116**, 933-943 (2026).
476 37. Filhol, J.-S. & Neurock, M. Elucidation of the electrochemical activation of water
477 over Pd by first principles. *Angew. Chem. Int. Ed.* **45**, 402–406 (2006).
478 38. Duan, Z. & Henkelman, G. Theoretical resolution of the exceptional oxygen
479 reduction activity of Au(100) in alkaline media. *ACS Catal.* **9**, 5567–5573 (2019).
480 39. She, Z. W. et al. Combining theory and experiment in electrocatalysis: insights into
481 materials design. *Science* **355**, eaad4998 (2017).
482 40. Fairhurst, A. R., Snyder, J., Wang, C., Strmcnik, D. & Stamenkovic, V. R.
483 Electrocatalysis: from planar surfaces to nanostructured interfaces. *Chem. Rev.* **125**,
484 1332–1419 (2025).
485 41. Chen, H., Wang, L., Na, M. & Zou, X. Reconstruction chemistry of electrocatalysts
486 under working conditions. *Chem. Sci.* **16**, 20662–20676 (2025).
487 42. Choi, J. & Aurbach, D. Promise and reality of post-lithium-ion batteries with high
488 energy densities. *Nat. Rev. Mater.* **1**, 16013 (2016).
489 43. Bruce, P. G., Freunberger, S. A., Hardwick, L. J. & Tarascon, J.-M. Li–O_2 and Li–
490 S batteries with high energy storage. *Nat. Mater.* **11**, 19–29 (2012).

44. Wang, L. et al. The promises, challenges and pathways to room-temperature sodium-sulfur batteries. *NatI. Sci. Rev.* **9**, nwab050 (2021).
45. Kresse, G. & Furthmüller, J. Efficient iterative schemes for ab initio total-energy calculations using a plane-wave basis set. *Phys. Rev. B* **54**, 11169–11186 (1996).
46. Kresse, G. & Joubert, D. From ultrasoft pseudopotentials to the projector augmented-wave method. *Phys. Rev. B* **59**, 1758–1775 (1999).
47. Blöchl, P. E. Projector augmented-wave method. *Phys. Rev. B* **50**, 17953–17979 (1994).
48. Kresse, G. & Joubert, D. From ultrasoft pseudopotentials to the projector augmented-wave method. *Phys. Rev. B* **59**, 1758–1775 (1999).
49. Perdew, J. P., Burke, K. & Ernzerhof, M. Generalized gradient approximation made simple. *Phys. Rev. Lett.* **77**, 3865–3868 (1996).
50. Grimme, S., Antony, J., Ehrlich, S. & Krieg, H. A consistent and accurate ab initio parametrization of density functional dispersion correction (DFT-D) for the 94 elements H-Pu. *J. Chem. Phys.* **132**, 154104 (2010).
51. Grimme, S., Ehrlich, S. & Goerigk, L. Effect of the damping function in dispersion corrected density functional theory. *J. Comput. Chem.* **32**, 1456–1465 (2011).
52. Xu, H., Cheng, D., Cao, D. & Zeng, X. C. Revisiting the universal principle for the rational design of single-atom electrocatalysts. *Nat. Catal.* **7**, 207–218 (2024).
53. Li, X. et al. Direct visualization of the Jahn–Teller effect coupled to Na ordering in $Na_{5/8}MnO_2$. *Nat. Mater.* **13**, 586–592 (2014).
54. Monkhorst, H. J. & Pack, J. D. Special points for Brillouin-zone integrations. *Phys. Rev. B* **13**, 5188-5192 (1976).
55. Henkelman, G., Arnaldsson, A. & Jónsson, H. A fast and robust algorithm for Bader decomposition of charge density. *Comput. Mater. Sci.* **36**, 354-360 (2006).
56. Tang, W., Sanville, E. & Henkelman, G. A grid-based Bader analysis algorithm without lattice bias. *J. Phys.: Condens. Matter* **21**, 084204 (2009).
57. Mathew, K., Sundararaman, R., Letchworth-Weaver, K., Arias, T. A. & Hennig, R. G. Implicit solvation model for density-functional study of nanocrystal surfaces

and reaction pathways. *J. Chem. Phys.* **140**, 084106 (2014).

58. Mathew, K., Kolluru, V. S. C., Mula, S., Steinmann, S. N. & Hennig, R. G. Implicit self-consistent electrolyte model in plane-wave density-functional theory. *J. Chem. Phys.* **151**, 234101 (2019).

Acknowledgements

This work was supported by the Zhejiang Provincial Natural Science Foundation of China (LMS25B030009), the Basic Research Project of WenZhou City (G20240018), the National Natural Science Foundation of China (22679147), the Key Research and Development Program of Zhejiang Province (2024C01057, 2025C01155), Central Government Guidance Fund for Local Science and Technology Development (2025ZY01041), Program of Zhejiang Provincial Key Laboratory of Advanced Battery Materials and Technology (2025E10124).

Author contributions

X. T. supervised the project. X. T., L. K., S. C. and X. W. conceived the idea and designed the research. X. T. performed all the calculations. T. L., P. T., D. L., Q. W., X. W. and Y. D. participated in discussions analyzing the data obtained from the calculations. X. T. wrote the manuscript with input from all co-authors. All authors commented on and reviewed the manuscript.

Competing interests

The authors declare no competing interests.

Additional information

Supplementary information The online version contains supplementary material available at https://doi.org/.

Figure captions

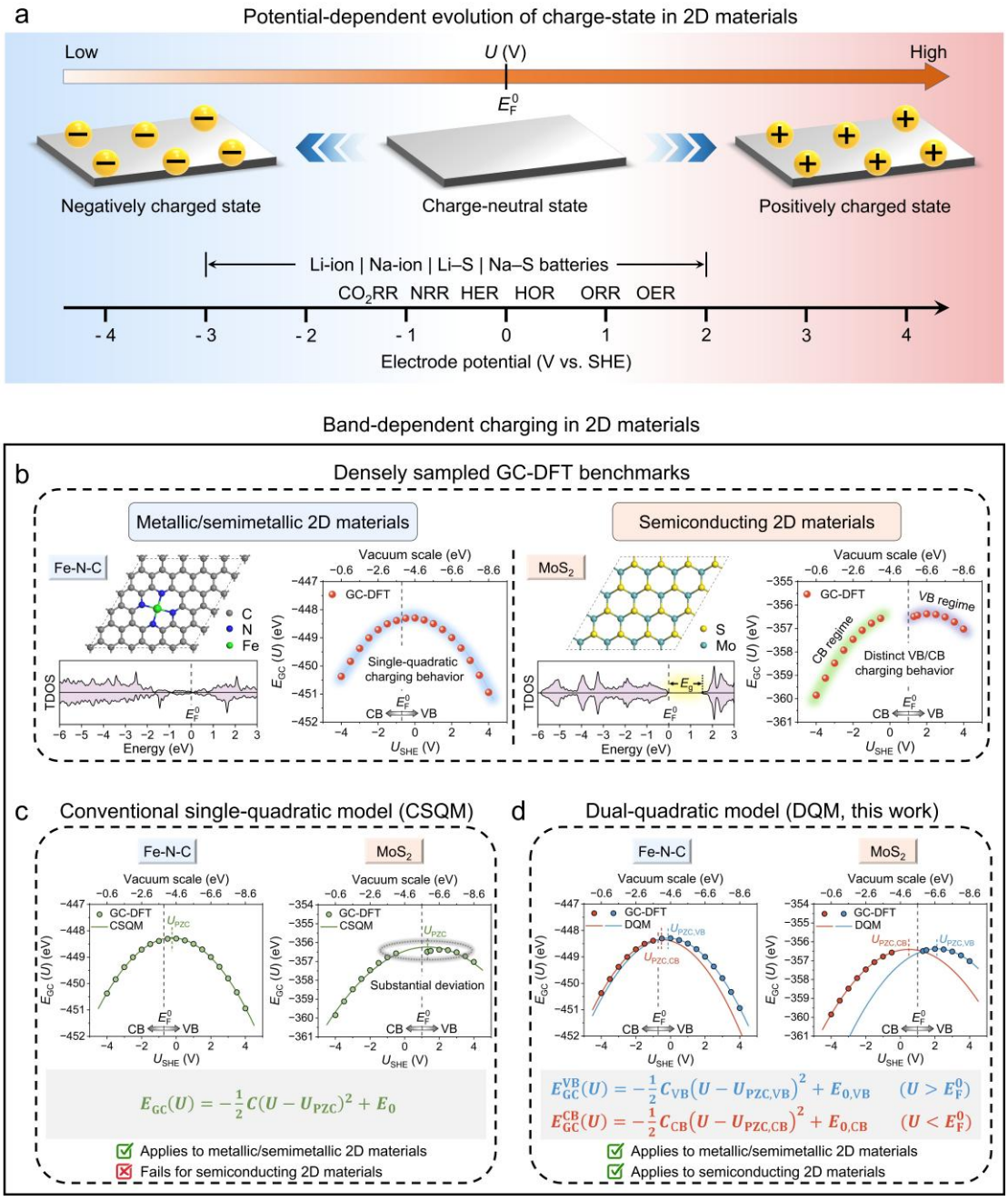


Fig. 1 | Band-dependent charging in 2D materials with contrasting intrinsic electronic characteristics. a, Schematic illustration of the potential-dependent evolution of charge states (top) and potential regimes relevant to electrochemical processes in electrocatalysis and rechargeable batteries (bottom). **b–d,** $E_{GC} - U$ relationships for semimetallic Fe–N–C and semiconducting MoS_2, obtained from densely sampled GC-DFT calculations (**b**) and predicted by the CSQM (**c**) and DQM (**d**). Atomic structures and total density of states (TDOS) are also shown in **b**. VB and CB denote the valence and conduction bands, respectively. Densely sampled GC-DFT

calculations establish reliable benchmarks, revealing contrasting manifestations of band-dependent charging: Fe–N–C exhibits effectively single-quadratic charging behavior, whereas MoS_2 displays distinct VB/CB charging behaviors. The CSQM reproduces the benchmark relationship for Fe–N–C but fails to capture the distinct VB/CB charging behaviors in MoS_2, whereas the DQM reproduces the benchmark relationships for both systems.

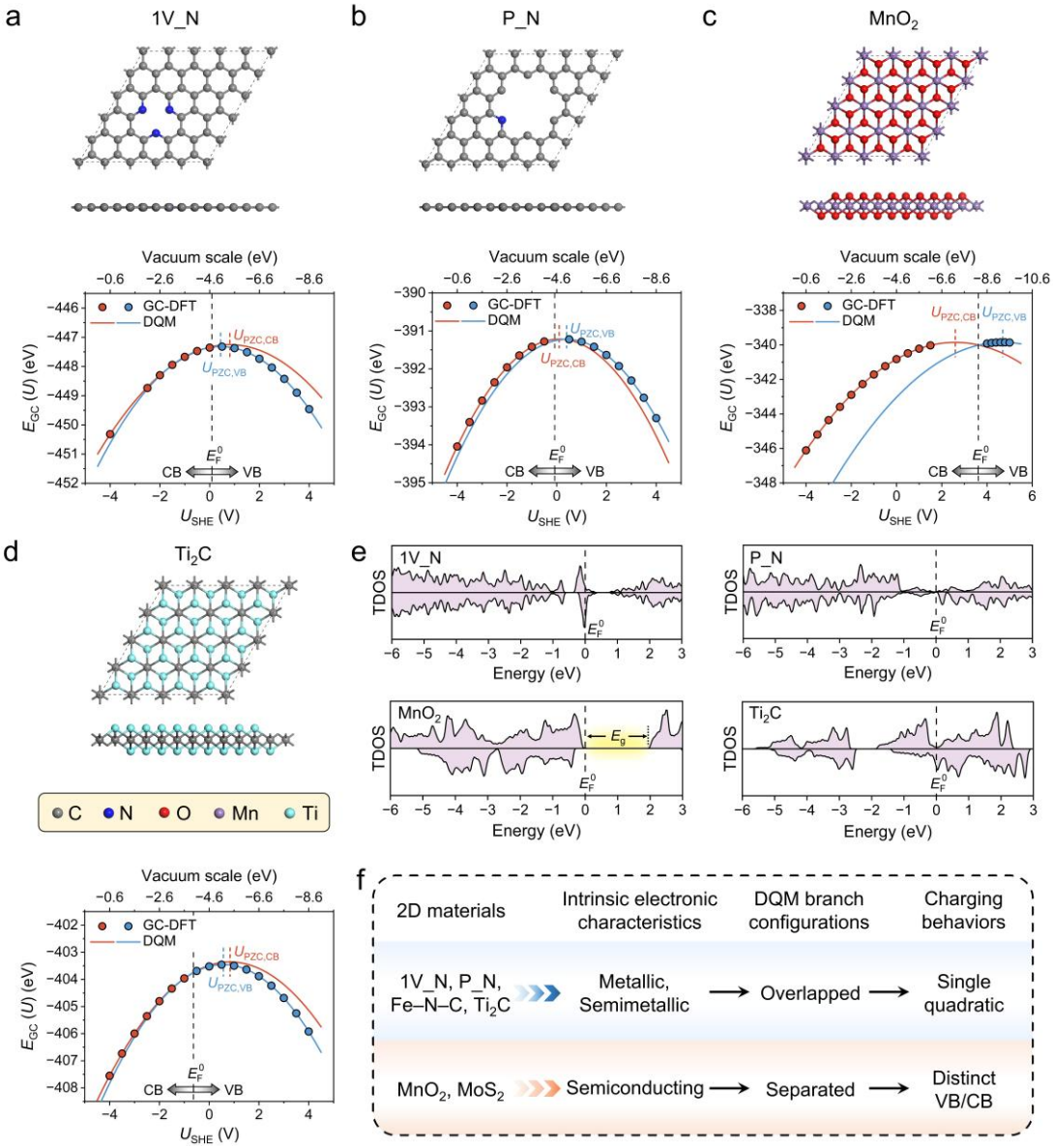


Fig. 2 | General applicability of the DQM for band-dependent charging across 2D materials with diverse intrinsic electronic characteristics. a–d, Atomic structures (top) and comparisons of DQM predictions with densely sampled GC-DFT benchmarks for the $E_{GC} - U$ relationships (bottom) of 1V_N (**a**), P_N (**b**), MnO_2 (**c**), and Ti_2C (**d**). The DQM reproduces the benchmark relationships across all four systems. VB and CB denote the valence and conduction bands, respectively. **e**, Total density of states (TDOS) of the four materials. **f**, Two manifestations of band-dependent charging: separated VB/CB branches in semiconductors versus overlapping branches in metallic/semimetallic systems, yielding effectively single-quadratic charging behavior.

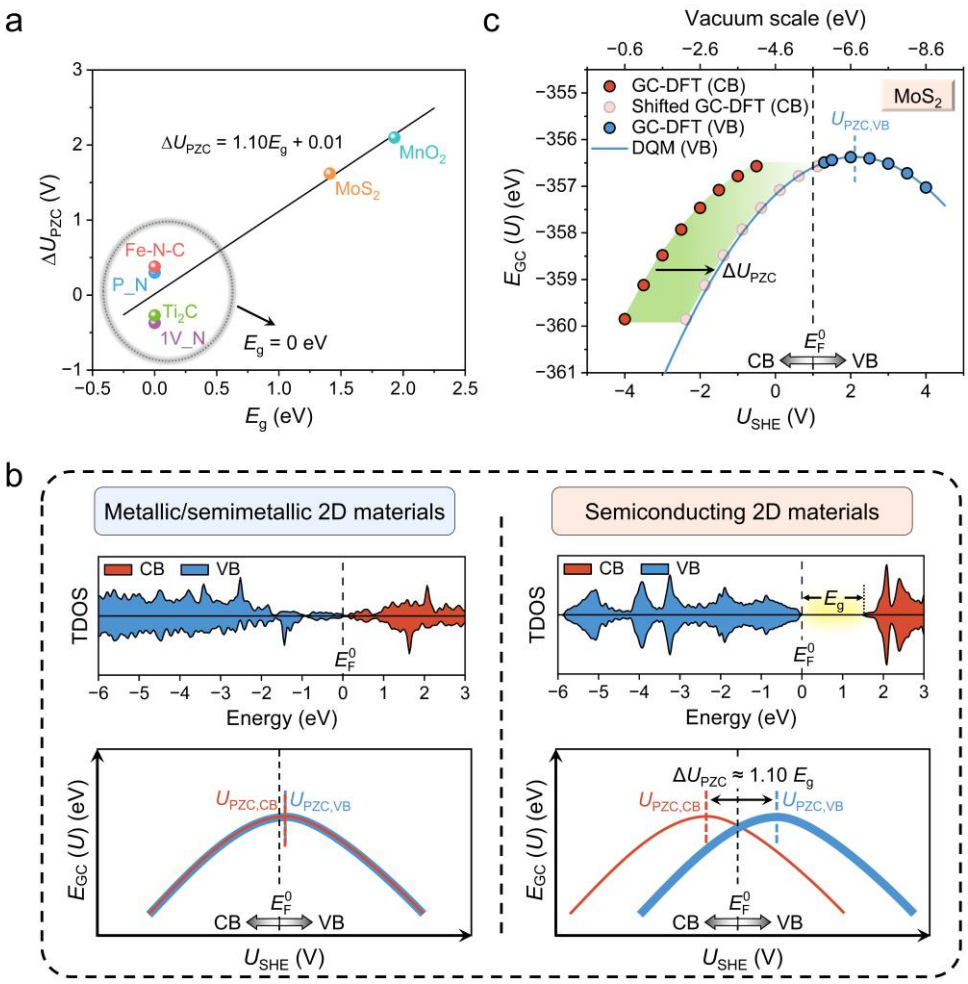


Fig. 3 | Electronic origin of band-dependent charging. a, Correlation between ΔU_{PZC} and E_{g} across different 2D materials. E_{g} is extracted from the calculated TDOS. ΔU_{PZC} exhibits an approximately linear dependence on E_{g}, with a slope of ~1.10. **b,** Schematic illustration of band-dependent charging in 2D materials with different intrinsic electronic characteristics. In semiconductors, a finite E_{g} corresponds to a non-negligible ΔU_{PZC}, separating the valence- and conduction-band branches along the potential axis. In metallic/semimetallic materials, the vanishing E_{g} is accompanied by a negligible ΔU_{PZC}, causing the two DQM branches to nearly overlap and exhibit effectively single-quadratic charging behavior, as described by the CSQM. **c,** Collapse of the valence- and conduction-band branches for MoS_2 onto a single quadratic dependence by shifting the conduction-band branch along the potential axis by ΔU_{PZC}.

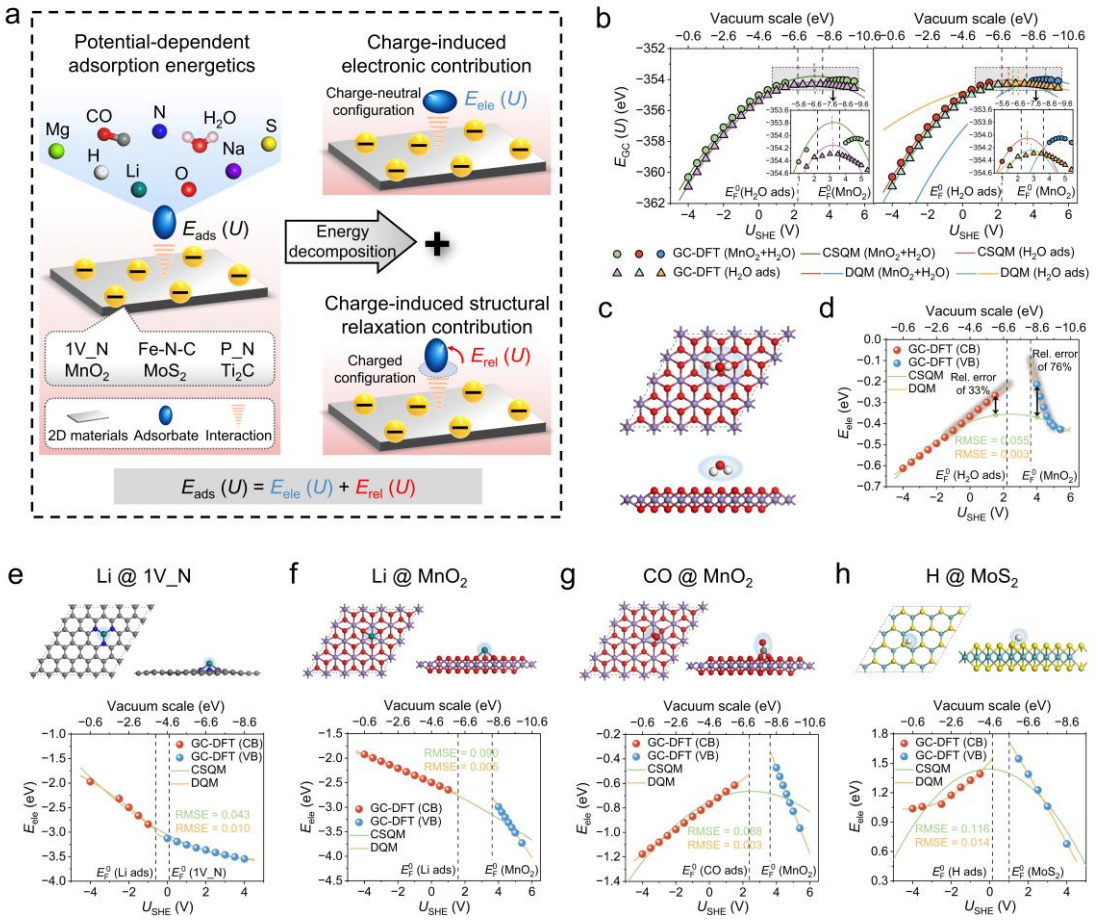
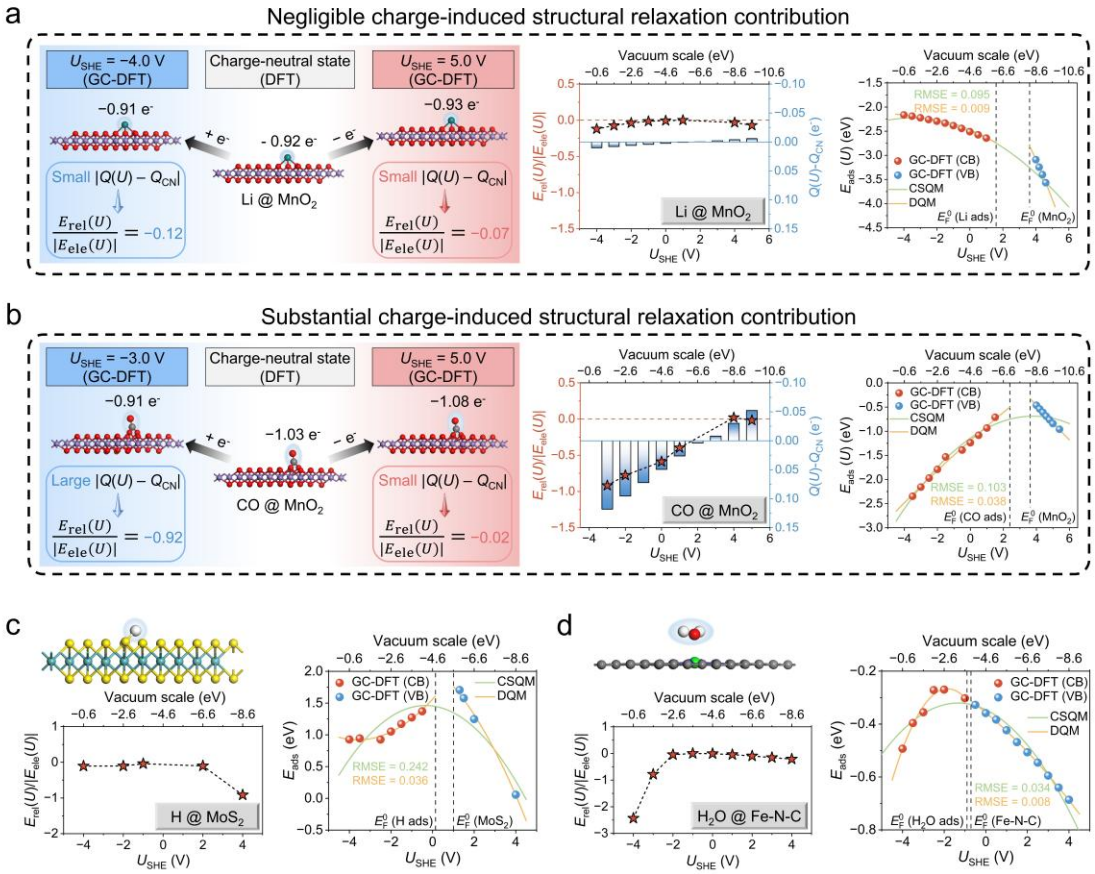


Fig. 4 | DQM prediction of charge-induced electronic contributions to potential-dependent adsorption energetics. a, Schematic illustration of the decomposition of potential-dependent adsorption energy ($E_{\mathrm{ads}}(U)$) into charge-induced electronic ($E_{\mathrm{ele}}(U)$) and structure relaxation ($E_{\mathrm{rel}}(U)$) contributions. **b,** DQM- and CSQM-predicted $E_{\mathrm{GC}} - U$ relationships for bare and H_2O-adsorbed MnO_2, compared with densely sampled GC-DFT benchmarks. **c**, Atomic structure of H_2O-adsorbed MnO_2. **d**, DQM- and CSQM-predicted $E_{\mathrm{ele}}(U)$ profiles for H_2O adsorption on MnO_2, compared with the benchmark profiles. **e–h**, Atomic structures (top) and $E_{\mathrm{ele}}(U)$ profiles (bottom) for Li adsorption on 1V_N (**e**), Li adsorption on MnO_2 (**f**), CO adsorption on MnO_2 (**g**), and H adsorption on MoS_2 (**h**). DQM and CSQM predictions are compared with the benchmark $E_{\mathrm{ele}}(U)$ profiles. RMSE values (eV) are provided in panels **d**–**h**.



599 **Fig. 5 | DQM prediction of potential-dependent adsorption energetics**
600 **incorporating charge-induced electronic and structural relaxation contributions.**
601 **a,b,** Li (**a**) and CO (**b**) adsorption on MnO_2. Left, charge-induced structural changes
602 under positive and negative potentials; middle, structural relaxation contributions
603 $(E_{\mathrm{rel}}(U)/|E_{\mathrm{ele}}(U)|)$ and potential-dependent deviations of the adsorbate charge from
604 its charge-neutral state $(Q(U) - Q_{\mathrm{CN}})$; right, comparison of DQM- and CSQM-
605 predicted $E_{\mathrm{ads}}(U)$ profiles with densely sampled GC-DFT benchmarks. Li exhibits
606 negligible structural relaxation across the full potential range, whereas CO undergoes
607 pronounced structural relaxation induced by charging. **c,d,** Additional systems with
608 substantial structural relaxation contributions: H adsorption on MoS_2 (**c**) and H_2O
609 adsorption on Fe–N–C (**d**). Upper left, atomic structures; lower left, $E_{\mathrm{rel}}(U)/|E_{\mathrm{ele}}(U)|$
610 profiles; right, comparison of DQM- and CSQM-predicted $E_{\mathrm{ads}}(U)$ profiles with
611 densely sampled GC-DFT benchmarks. RMSE values are given in eV.
612
613

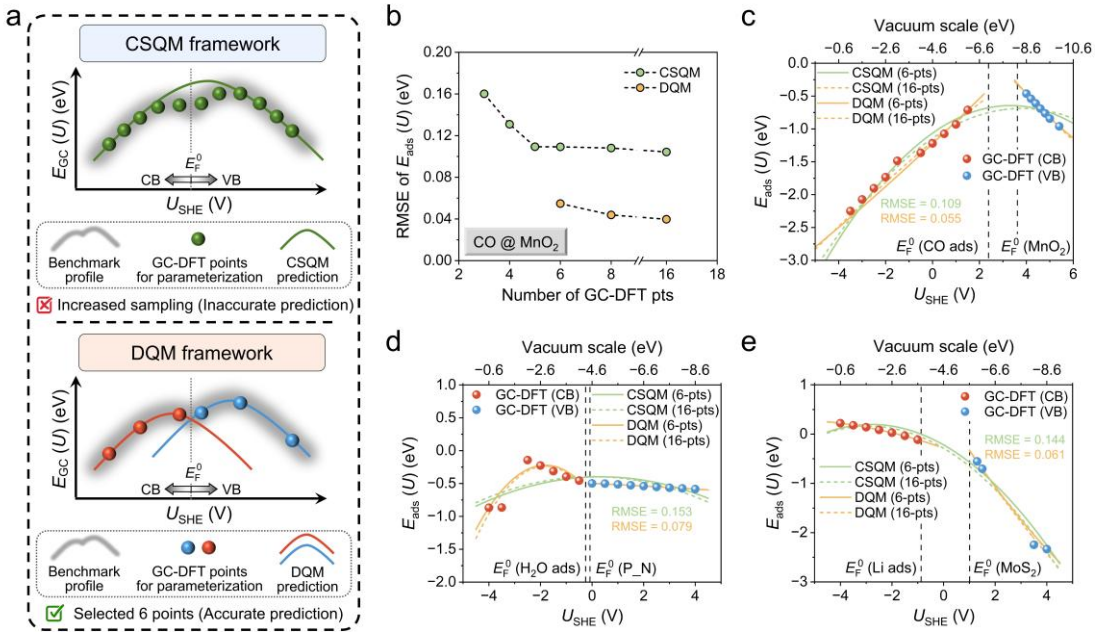


Fig. 6 | Efficient prediction of potential-dependent adsorption energetics from sparse GC-DFT sampling. a, Schematic illustration of DQM and CSQM parameterization using sparse GC-DFT sampling. **b**, RMSE of DQM- and CSQM-predicted $E_{\mathrm{ads}}(U)$ as a function of the number of discrete GC-DFT calculations used for parameterization. The 6-point DQM achieves high predictive accuracy (RMSE ~ 0.055 eV), whereas the CSQM retains an RMSE of 0.104 eV even with 16 sampling points. **c,** Comparison of the 6-point and 16-point DQM-predicted $E_{\mathrm{ads}}(U)$ profiles with the benchmark profile for CO adsorption on MnO_2. The two DQM predictions nearly overlap and reproduce the benchmark profile across the full potential range. **d,e,** Applicability of the 6-point DQM to H_2O adsorption on P_N (**d**) and Li adsorption on MoS_2 (**e**). In **c**–**e**, the corresponding 6-point and 16-point CSQM predictions are also shown for comparison, and RMSE values (eV) for the 6-point DQM and CSQM predictions are provided.

Supplementary Files

This is a list of supplementary files associated with this preprint. Click to download.

- SupplementaryInformation10.24.docx